

Heuristic Weakly Supervised 3D Human Pose Estimation

Shuangjun Liu · Michael Wan · Sarah Ostadabbas

Received: date / Accepted: date

Abstract Monocular 3D human pose estimation from RGB images has attracted significant attention in recent years. However, recent models depend on supervised training with 3D pose ground truth data or known pose priors for their target domains. 3D pose data is typically collected with motion capture devices, severely limiting their applicability. In this paper, we present a heuristic weakly supervised 3D human pose (HW-HuP) solution to estimate 3D poses in when no ground truth 3D pose data is available. HW-HuP learns partial pose priors from 3D human pose datasets and uses easy-to-access observations from the target domain to estimate 3D human pose and shape in an optimization and regression cycle. We employ depth data for weak supervision during training, but not inference. We show that HW-HuP meaningfully improves upon state-of-the-art models in two practical settings where 3D pose data can hardly be obtained: human poses in bed, and infant poses in the wild. Furthermore, we show that HW-HuP retains comparable performance to cutting-edge models on public benchmarks, even when such models train on 3D pose data¹.

Keywords Monocular 3D pose estimation · Weakly supervised learning · Optimization · Infant poses · In-bed poses.

1 Introduction

Applied machine learning (ML) researchers have repeatedly come up against the problem of data scarcity in practical settings. Data-efficient methods, which exploit structural knowledge in each domain to constrain models to being simple

S. Liu, M. Wan and S. Ostadabbas
Augmented Cognition Lab, Electrical and Computer Engineering Department, Northeastern University.

¹ Our model code and data are publicly available at <https://github.com/ostadabbas/hw-hup>.

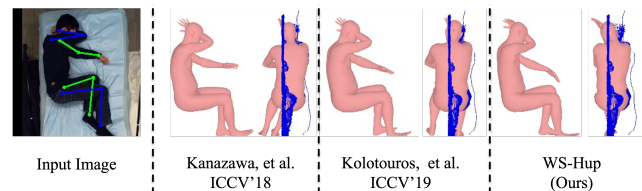


Fig. 1: Predictions from SOTA 3D human pose and shape estimation models compared to our heuristic weakly-supervised 3D human pose estimation (HW-HuP) model, on an in-bed pose image taken from the SLP dataset (Liu et al., 2023). All models have been fine-tuned on SLP data. Viewed from the top, all three models perform well, but the side view shows that the HW-HuP estimation is more precise in a number of ways. Point clouds from the depth data are rendered in blue for reference.

enough to train with the available data (Dai et al., 2007), have emerged in response. However, data-efficient ML often requires at least *some* sample data from the target domain, or, in the case of zero-shot learning (Romera-Paredes and Torr, 2015), some shared attributes in the source and target domains. But what can be done if context constraints entail that not even a single annotated sample is available for a target application?

Our paper addresses this challenge for the task of 3D human pose estimation in the wild, where no ground truth 3D pose data are accessible and known priors do not exist. We present a transfer learning approach based on a heuristic weakly supervised framework with depth data as surrogate 3D information. Our work focuses on applications where techniques based on the motion capture (MoCap) systems—which involve specialized markers, multiple cameras, and controlled environments—are not feasible, even for gathering training data. These contexts might include hospital patient behavior monitoring, as studied by our lab (Liu et al., 2023) and others (Clever et al., 2020), or infant in the crib activity monitoring (Hesse et al., 2017). Fig. 1 demonstrates

the qualitative limitations of state-of-the-art (SOTA) 3D pose estimation models for in-bed patient monitoring—an application critically in need of automation, as highlighted by the recent global pandemic.

In place of 3D data from MoCap, we assume that training data is captured with an inexpensive, off-the-shelf RGBD camera, which adds depth information to 2D RGB data (Zimmermann et al., 2018). Note, that RGBD data does not directly provide 3D joint locations, as the depth cloud generally lies on the surface of the body, and this discrepancy is exaggerated for limbs occluded by other body parts. Existing approaches offer plausible solutions for human mesh tracking and recovery from RGBD data, but typically have requirements which limit their general applicability: (Hassan et al., 2019) needs a static scan of the environment; (Hesse et al., 2019) assumes that the subject is lying on a flat, decluttered surface, and requires sequential RGBD data for training; (Bogo et al., 2015) requires a static background where the subject point cloud can be cleanly segmented, and also sequential data; and (Zimmermann et al., 2018) requires depth data during inference. By contrast, our method is trained on single RGBD images, makes inferences on single RGB images, and is free from environmental requirements. Our heuristic weakly supervised 3D human pose estimation model (HW-HuP) is trained using both the learned pose and shape priors from public 3D pose datasets, as well as 2D pose and depth observations from the target domain. By partially learning the priors from the source domain and the noisy observations from the target domain, our approach iteratively converges to a reliable 3D pose estimation. The final product is a predictive model which can estimate 3D human pose and shape directly from a single 2D image taken in the wild (camera calibration parameters are neither needed nor assumed).

Our results show that HW-HuP performs robustly in real-world scenarios where 3D pose data is not available, such as with individuals in bed, or infants moving freely in cribs or playrooms. We also show that HW-HuP retains strong performance under different input modalities, such as pressure map, depth, or infrared signals. Finally, HW-HuP exhibits performance comparable to SOTA methods on public benchmarks in the lab and in the wild, even when those methods take advantage of full 3D ground truth data in training and HW-HuP does not.

2 Related Work

RGB-based 3D Human Pose Estimation: While we focus our attention here on 3D human pose estimation from RGBD images, there has naturally been extensive work on such estimation from RGB images. These run the gamut from end-to-end methods (Mehta et al., 2017; Park et al., 2016; Pavlakos et al., 2017; Rogez et al., 2017), to lifting 2D

estimations to 3D (Zhou et al., 2015; Chen and Ramanan, 2017; Tung et al., 2017; Rhodin et al., 2018). Our model draws on work from (Bogo et al., 2016), which directly regresses the pose and shape parameters from a learned template.

RGBD-based 3D Human Pose Estimation: Some techniques successfully use RGBD data to predict human poses, including detailed body meshes (De Aguiar et al., 2007; Bogo et al., 2015; Li et al., 2019). The popular Microsoft Kinect RGBD camera even includes a 3D pose estimator in its software development kit (SDK), so it is tempting to conclude that RGBD data is sufficient for 3D human pose estimation in general. However, in practice, these methods have significant constraints, restricting their application to controlled environments. For example, for full body mesh reconstruction, continuous depth data is often required; initialization poses, cleanly segmented point clouds, are sometimes needed in (Helten et al., 2013; Ye and Yang, 2014; Lan et al., 2012; Yu et al., 2017; Hesse et al., 2019); and static scans of the empty environment are requisite in (Hassan et al., 2019). Single frame depth estimation approaches do exist, but they fail on novel applications (Liu et al., 2023) and still require ground truth 3D pose or segmentation annotations (Shotton et al., 2011; Haque et al., 2016; Xiong et al., 2019).

3 Method

This paper focuses on 3D human pose estimation when for training only RGBD data is accessible and during inference only RGB data is available. In order to separate our 3D pose estimation task from the 2D problem, we assume that the 2D poses are given—either from an effective 2D pose estimator, or refined with human input from a baseline 2D pose estimator using the AI human co-labeling toolbox (Huang et al., 2019) developed by our lab.

In sum, the following *data availability* is assumed: (1) 2D image data I (RGB, unless otherwise specified); (2) depth data D ; (3) a 2D pose ground truth annotation x_{gt} ; and (4) a 3D pose estimation model F pre-trained on large-scale publicly-available 3D human pose datasets. Since we are targeting applications in natural settings, we also assume the following *data constraints* on the depth D : (1) D is available during training but not inference; (2) D may not be continuous across frames; and (3) D might be so noisy that the subject cannot be easily segmented from the background.

By combining 2D joint x and the depth D , we have *depth-based proxy 3D coordinates* X_{dp} , which is actually different from the true joint location. Setting aside irreducible error stemming from the noisiness of D , there are two fundamental and nonuniform sources of bias for these depth-based proxy 3D coordinates, which depend on pose and shape. First, proxy 3D coordinates will sit on the surface of a body,

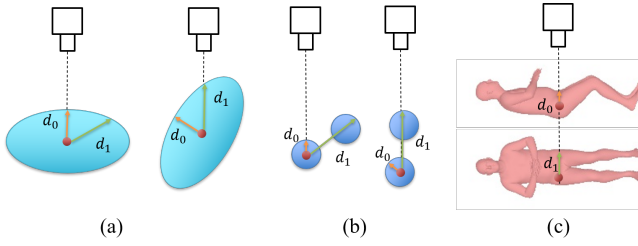


Fig. 2: Depth proxy point bias from the true joint location in: (a) a single body with uneven shape, (b) double bodies with occlusion, and (c) right hip of a human body.

whereas the true 3D skeletal joint coordinates reside inside the body. Critically, this offset may not be uniform across joints due to shape and pose differences, as illustrated for the idealized human limb in Fig. 2(a). We refer to the resulting error as a **Type 1 error**. Another source of bias stems from body parts overlapping in such a way that one joint is occluded from the camera by another joint or body part, as with crossed arms or legs, and as illustrated ideally in Fig. 2(b) and more concretely in Fig. 2(c). This error is usually large across limbs, and is referred to as **Type 2 error**. Type 1 and Type 2 error distributions for each joint are provided in the *Supplementary Materials*.

3.1 HW-HuP Problem Formulation

Our objective is to obtain a 3D pose regression model F which takes in a single 2D image I and estimates 3D human pose parameters $\Theta = [\theta, \beta]$ and camera parameters C , via $F(I) = [\Theta, C]$. Following (Kolotouros et al., 2019a), we use the skinned multi-person linear model (SMPL) (Loper et al., 2015), with pose $\theta \in \mathbb{R}^{3K+3}$ representing the relative rotation angles of $K = 23$ body parts with respect to their parents in the kinematic tree, plus the root global rotation, and shape $\beta \in \mathbb{R}^P$ representing the first $P = 10$ principle components analysis (PCA) coefficients of the human template space. The SMPL model is a differential function that outputs a triangulated mesh $M(\Theta) \in \mathbb{R}^{3 \times N}$ with $N = 6980$ vertices. The camera model $C = [T, s]$ includes a translation vector $T \in \mathbb{R}^2$ and a scale $s \in \mathbb{R}$. For a given pose Θ (sometimes implicitly including C), each 3D keypoint $X(\Theta) \in \mathbb{R}^3$, is a fixed linear combination of the vertices from the mesh $M(\Theta)$ (Kolotouros et al., 2019a). Its 2D projection x is given by $x = s\Phi(RX(\Theta)) + T$, where Φ is an orthographic projection and R is the global rotation matrix $R \in \mathbb{R}^{3 \times 3}$, both derived from C .

3.2 HW-HuP Model Description

HW-HuP extends SPIN (Kolotouros et al., 2019b), by incorporating depth data into the supervision in two stages in

a coarse-to-fine manner. HW-HuP assimilates source priors differently, and allows for input modalities beyond RGB. Recapping the SPIN work, we have the human pose and shape regression model F with output of SMPL parameters $F(I) = \Theta_{\text{reg}}$ and corresponding 2D joints x_{reg} might be trained with supervision from ground truth 2D joints x_{gt} via the loss function

$$L_{2D}(\Theta_{\text{reg}}) := \sum_{\text{joints } j} \|x_{\text{reg}}(j) - x_{\text{gt}}(j)\|_2^2. \quad (1)$$

The key idea behind SPIN is to instead use the ground truth 2D joint data x_{gt} to fit the model $M(\Theta_{\text{reg}})$ to the image I via an iterative optimization procedure called SMPLify (Bogo et al., 2016), and then using the resulting optimized model parameter Θ_{opt} to supervise F via the loss function

$$L_{\text{SPIN}}(\Theta_{\text{reg}}) := \|\Theta_{\text{reg}} - \Theta_{\text{opt}}\|_2^2. \quad (2)$$

The loop $I \mapsto \Theta_{\text{reg}} \mapsto \Theta_{\text{opt}}$ represents a single SPIN forward step, and with mechanisms in place to discard bad optimization results, both the regression F and the SMPLify optimization improve “collaboratively” over time.

HW-HuP modifies SPIN by tweaking the SMPLify optimization procedure, and more importantly, by incorporating depth data into the supervision of the regression F in one of two ways depending on the training epoch, resulting in an overall loss function of

$$L_{\text{reg}}(\Theta_{\text{reg}}) := L_{2D}(\Theta_{\text{reg}}) + L_{\text{SPIN}}(\Theta_{\text{reg}}) + \begin{cases} L_{3D}(\Theta_{\text{reg}}) & \text{in Stage I} \\ L_{\text{depth}}(\Theta_{\text{reg}}) & \text{in Stage II} \end{cases} \quad (3)$$

(with L_{2D} included following the SPIN implementation). We now turn to detailed descriptions of each modification that HW-HuP makes to SPIN with an overview shown in Fig. 3.

Selective Pose Prior Transfer (Optimization): The iterative optimization used in SPIN is a modified version of the SMPLify algorithm (Bogo et al., 2016). It takes the regressed pose prediction Θ_{reg} (here, including C_{reg}) as initial input and outputs an optimized Θ_{opt} after a number of internal steps, all within a single forward pass of each SPIN training step. The modified SMPLify algorithm first optimizes the camera parameter $C_{\text{reg}} \mapsto C_{\text{opt}}$, and then optimizes $\Theta_{\text{reg}} \mapsto \Theta_{\text{opt}}$ via a multi-step iterative process guided by the objective loss function

$$L_{\text{opt}}(\Theta_{\text{opt}}) := L_{2D}(\Theta_{\text{opt}}) + \lambda_{\theta} L_{\theta}(\theta_{\text{opt}}) + \lambda_{\beta} L_{\beta}(\beta_{\text{opt}}) + \lambda_{\alpha} L_{\alpha}(\theta_{\text{opt}}), \quad (4)$$

where L_{2D} is the 2D joint loss, L_{θ} is GMM pose prior learned from the source domain, L_{β} is a quadratic penalty on the shape coefficients, L_{α} is an unnatural joint rotation penalty of elbows and knees, and λ_{θ} , λ_{β} , and λ_{α} are scalar constants. HW-HuP modifies the coefficient $\lambda_{\theta} = \lambda_{\theta,0} f^e$ to

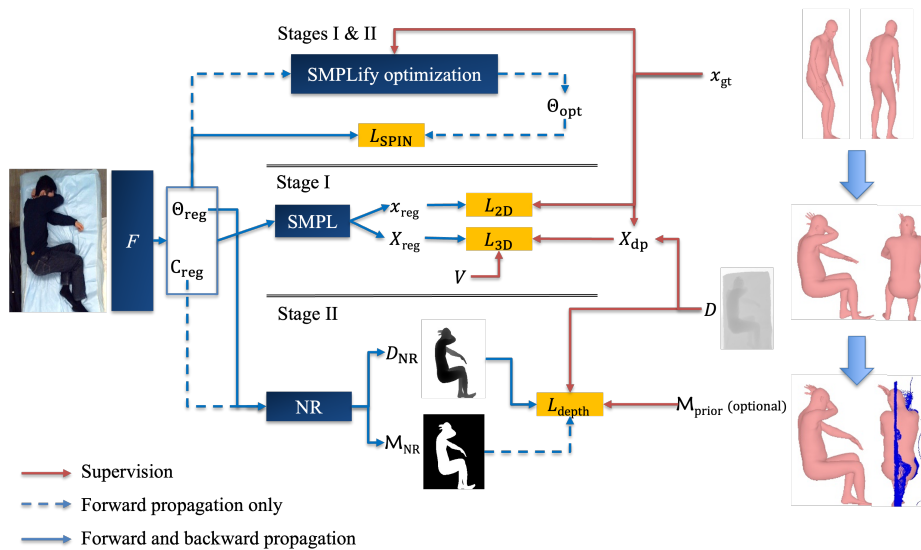


Fig. 3: HW-HuP framework. In each step, HW-HuP trains the 3D pose regression function F by supervising its pose predictions $[\Theta_{\text{reg}}, C_{\text{reg}}]$ with the outcome of the SMPLify 2D joint optimization, which incorporates heuristic prior information, as well as one of 3D based pipelines depending on the stage. In Stage I, HW-HuP uses coarse, depth based proxy 3D coordinates for the joints to supervise predicted joint positions, attenuated by visibility V to ensure correct alignment of obscured limbs. After Stage I, the 2D joints and silhouette should be nearly aligned and the 3D pose acceptable. In Stage II, HW-HuP fine-tunes the 3D pose using the full depth map D to supervise a depth map D_{NR} generated by passing the predicted pose through a neural renderer NR, attenuated by a generated mask \mathcal{M}_{NR} and an *optional* mask prior $\mathcal{M}_{\text{prior}}$ if available.

introduce an exponential decay of strength f over epoch e from the initial $\lambda_{\theta,0}$ weight for the GMM prior. As the source prior fades over time, the major body parts tend to become increasingly guided by incoming target data, but the influence the source prior is retained for small body parts.

Coarse 3D Pose-Based Supervision (Stage I): In Stage I, we want to supervise the regression F by penalizing differences between its 3D joint predictions X_{reg} and the true 3D joint locations, but these are unknown. What we do have are the depth-based proxy 3D coordinates, X_{dp} , but these can be biased away from the true 3D joint locations, with significant variation as illustrated in Fig. 2. To remedy the most egregious Type 2 errors stemming from occlusion, we design and train a visible joint detection model V and use it to construct our weakly supervised 3D pose loss:

$$L_{3\text{D}}(\Theta_{\text{reg}}) = \sum_{\text{joints } j} V(j) \|X_{\text{reg}}(j) - X_{\text{dp}}(j)\|_2^2, \quad (5)$$

where $V(j)$ is the visibility for joint j . The idea is that in cases of heavy occlusion of j , a low visibility prevents $X_{\text{dp}}(j)$ from sending the potentially wrong signal in the backward pass. The regressor F instead learns the 3D location of that occluded joint by inferring from nearby poses where that joint is more visible. Our visible joint detection model V is obtained by fine-tuning a SOTA pose estimation model and adding a visible joint detection branch called VisNet. Details are provided in *Supplementary Material*. In cases where visibility annotations are provided for 2D joints we use them directly for V .

Fine Depth-Based Supervision (Stage II): In Stage I, the 2D joint data x and source prior supervision ensure that our model yields a plausible frontal view with aligned 2D poses, and the 3D proxy joint X_{dp} supervision ensures that the estimated joints will be close to their true locations in 3D space, with most Type II errors reduced. However, small bias introduced by Type I errors still remain. In Stage II, we take advantage of successful 2D and 3D alignments in Stage I to enable fine-grained depth supervision with the full depth data D to further refine the estimation F and reduce Type I errors. To do this, we employ a differential neural renderer (NR) (Kato et al., 2018), which takes in the estimated 3D body mesh $M(\Theta_{\text{reg}})$ and returns the corresponding depth map D_{NR} to align with the observed depth D . After stage I alignment, the discrepancies only exist over the silhouette of the body, thus, we also make use of the estimated silhouette, or 2D mask $\mathcal{M} = \mathcal{M}_{\text{NR}}$, which is provided by the neural renderer. If a prior mask $\mathcal{M}_{\text{prior}}$ is available—such as an annotated ground truth mask or a weak estimate like a bounding cubic indicating the foreground area—we work with its intersection with the neural renderer prediction: $\mathcal{M} = \mathcal{M}_{\text{NR}} \cap \mathcal{M}_{\text{prior}}$. The fine depth loss for Stage II is thus

$$L_{\text{depth}}(\Theta_{\text{reg}}) = \|D - b_0 - D_{\text{NR}}\|_{2, \mathcal{M}}^2, \quad (6)$$

where $\|\cdot\|_{2, \mathcal{M}}$ is the L^2 norm taken over pixels in \mathcal{M} only, and b_0 is a correction factor for the bias introduced by using imaginary focal length, which minimizes the average distance from the observed depth D to the rendered depth D_{NR} :

$$b_0 = \arg \min_b \|D - b - D_{\text{NR}}\|_{2, \mathcal{M}}. \quad (7)$$

Since our D is smoothed and filtered, we use the L^2 norm in L_{depth} , but in cases of noisy D or with many outliers, we recommend using a robust penalty loss such as German-McClure (Geman, 1987) instead.

4 Experimental Evaluation

4.1 Evaluation Datasets

We evaluate the performance of the HW-HuP framework with the following datasets. The first three are used to quantify real-world performance, in the absence of 3D pose annotations or priors.

SLP Dataset: The simultaneously-collected multimodal lying pose (SLP) dataset (Liu et al., 2023) was collected with IRB approval by our team under Northeastern University approval IRB #17-06-04, from seven participants in a hospital room and 102 participants in a living room. The four modalities of RGB, long wavelength infrared (LWIR), depth, and pressure map were simultaneously collected under three cover conditions: no cover (“Nocover”), a thin layer sheet (“Cover1”), and a thick blanket (“Cover2”). SLP does not have 3D pose annotations and exhibits a pose prior distinct from those found in popular pose datasets. Correspondingly, pre-trained SOTA models perform weakly on SLP (Liu et al., 2023) and there are limited works addressing the 3D human pose problem presented in SLP dataset (Clever et al., 2020), making it a useful real-world testing ground for our framework. Since there is no ground truth 3D pose data, we measure performance using the *aligned depth error*, defined as the mean of the distances (in mm) between the predicted D_{reg} and the provided ground truth $D = D_{\text{gt}}$, taken over the intersection of the predicted and ground truth silhouette masks, after camera alignment.

SyRIP (Huang et al., 2021): The synthetic and real infant pose (SyRIP) dataset, also developed by our team, combines the real (web-sourced) and synthetic infant images. We use the first 1600 images for training and the remaining 100 for testing.

MIMM: This privately-owned modeling infant motor movement (MIMM) dataset was collected by a medical startup company with collaborative institutional approval (as part of an NIH funded study), and contains video recordings of interactive motor assessment sessions from 68 infants under age one with their caregivers and clinicians. Depth data from an MS Kinect camera is provided.

The next two datasets are used to quantify the error in HW-HuP introduced by not using 3D pose ground truth data.

Human3.6M (Ionescu et al., 2013): A large-scale indoor daily activity MoCap benchmark for 3D human pose estimation. We employ Protocol#2 of the benchmark, where subjects S1, S5, S6, S7, S8 are used for training, and S9, S11 for testing.

3DPW (von Marcard et al., 2018): This dataset features mostly outdoor environments with poses captured via the Inertial Measurement Unit (IMU) sensors, and thus serves as a good benchmark for performance in the wild. We use it for evaluation only.

4.2 Implementation Details

Data Preparation: Depth data is preprocessed with denoising (Nguyen et al., 2012) and hole-filing (Liu et al., 2016) algorithms. The joint depth proxy X_{dp} is extracted from the 2D joint location x from the denoised depth image and re-projected into 3D in the camera space. All images are normalized cropped to center bodies. Random flipping, rotation, scaling, and random channel-wise noise are used for data augmentation.

Network Training: For the 3D regression F , we take the same design and initialization as in (Kolotouros et al., 2019a). We employ the differential neural renderer NR in (Kato et al., 2018). We follow the SMPLify and SPIN optimization loops used in (Kolotouros et al., 2019a; Bogo et al., 2016) and limit the max iterations to 50. All models are trained on an NVIDIA Tesla K40m with batch size 64. We employ Adam (Kingma and Ba, 2014) with learning rate 5×10^{-5} . For the SLP dataset, the model is trained in 30 total epochs, with Stage II starting at the tenth epoch. For Human3.6M, due to the high frame quantity and the near-repetition of poses in neighboring frames, we employed a downsampling rate of 50. Training takes four total epochs, with Stage II starting at the second epoch. For our infant model, we combine the SyRIP and MIMM datasets and train for a total of 640 epochs with Stage II starting at epoch 420.

4.3 Results and Ablation Study

We chose the SLP in-bed pose dataset to illustrate the effectiveness of HW-HuP in a domain with distinct and previously unknown pose priors. We start by considering images in the RGB modality where the subject is not covered by a bed sheet, to most closely match the testing conditions employed by other SOTA models (Kolotouros et al., 2019a; Kanazawa et al., 2018). For a fair comparison, we compare models which share the same input modality. This is also helpful to compare their general effect on different dataset later. We report the aligned depth error and also display some predictions in figures, across various configurations, to

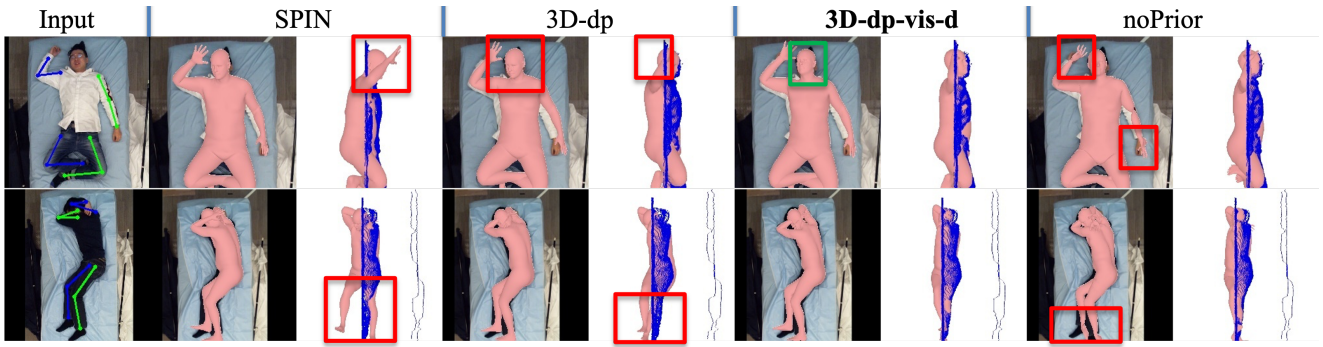


Fig. 4: Qualitative 3D human pose and shape estimation on SLP dataset using “Nocover” RGB images. The first row features the supine posture, and the second the side lying posture. Point clouds are shown as blue dots. Unnatural or bad predictions are outlined in red, and the particularly successful head pose prediction from HW-HuP (i.e. 3D-dp-vis-d in our ablation study) is outlined by the green rectangle.

Table 1: Aligned depth error (in mm) for 3D human pose and shape estimation predictions from SOTA models and HW-HuP configurations (for ablation), made on “Nocover” RGB images of the SLP dataset. Ablation studies defined in text.

SOTA Model				
SPIN*		SPIN		HMR
80.10		68.38		63.43
HW-HuP & Ablation Models				
3D-dp	3D-dp-vis	3D-dp-vis-D	noPrior	2D-D
48.13	47.41	36.01	38.54	39.32

highlight qualitative differences in performance. The SOTA models we compare with are:

- **SPIN***: Pretrained model from (Kolotouros et al., 2019a).
- **SPIN**: SPIN* fine tuned on SLP 2D pose training data.
- **HMR**: Pretrained model from (Kanazawa et al., 2018), fine tuned on SLP 2D pose training data.

We define configurations following simple plausible assumptions for our ablation study:

- **3D-dp (SMPLify + partial Stage I)**: *Assumption: 3D depth proxy is equivalent to the real 3D pose.* Supervise with just x_{gt} and X_{dp} , skipping Stage II.
- **3D-dp-vis (SMPLify + Stage I)**: *Test whether visibility helps by reducing the Type II errors.* Supervise with x_{gt} , X_{dp} , and visibility data V , skipping Stage II.
- **3D-dp-vis-D (full HW-HuP)**: The full HW-HuP model.
- **noPrior**: *Assumption: The source prior is not needed at all to train a model for target domain.* Set source prior constraint to zero.
- **2D-D (Stage II only)**: *Assumption: Fine-tuning directly with the available data is just as effective.* Remove SMPLify optimization loop; instead supervise F with only x_{gt} and D .

All models are trained with SLP “Nocover” RGB data, except the pretrained SPIN* model from (Kolotouros et al., 2019a). The resulting aligned depth errors (in mm) are reported in Table 1. Note that this metric can only partially represent the estimation quality as it cannot accurately quantify positions of occluded limbs. The results show that fine-tuning on the SLP data significantly improves SPIN performance compared to the purely pretrained SPIN*, but even then, SPIN and HMR perform notably worse than all HW-HuP models. Our ablation results show that depth proxy supervision (dp) by itself brings HW-HuP ahead of SPIN and HMR performance. Other model features such as the visibility supervision (V), full depth supervision (D), and source priors all further improve the model, with the best performance obtained by the full 3D-dp-vis-D. The good performance of the 2D-D configuration shows that straightforward supervision already leads to acceptable estimation, but in modalities other than RGB where no strong pretrained model is available, 2D-D performance is more limited.

Qualitative results for our experiment are presented in Fig. 4, which focuses on typical settings and representative issues. We highlight the tendency of SPIN (Kolotouros et al., 2019a) to adhere to the source prior for daily activities, as exemplified by the hands sticking out in supine and straddled legs in the side lying positions. 3D-dp is generally satisfactory for supine poses, which make sense since these poses typically exhibit less limb occlusion, eliminating the source of the largest depth proxy biases; but local defects like the slightly raised head and the legs bent into the bed remain. By contrast, all of these errors are handled by the full 3D-dp-vis-D. Without the source prior, major limbs are in good alignment, but small body parts are distorted.

4.4 Extending Inputs Beyond RGB

HW-HuP is designed to work well with modalities beyond the commonly-used RGB, which can be helpful under chal-

Table 2: Aligned depth error (in mm) of HW-HuP and SOTA 3D human pose and shape estimation on SLP dataset, under “Nocover”, “Cover1”, “Cover2” and “All Covers” conditions; and under depth, LWIR, PM, and their “Combined” modalities.

Nocover	Depth	LWIR	PM	Combined
SPIN*	108.78	89.41	102.27	96.13
HMR	68.70	69.20	75.70	72.55
SPIN	62.72	66.60	70.28	67.35
HW-HuP	33.87	38.45	41.48	37.62
Cover1	Depth	LWIR	PM	Combined
SPIN*	105.82	92.65	101.01	102.27
HMR	72.81	71.25	75.92	72.52
SPIN	67.71	67.81	70.29	67.96
HW-HuP	36.87	39.82	41.43	37.92
Cover2	Depth	LWIR	PM	Combined
SPIN*	105.34	89.31	101.08	100.82
HMR	73.06	70.69	76.10	73.11
SPIN	68.38	66.58	70.40	68.15
HW-HuP	37.26	40.42	41.68	38.26
All Covers	Depth	LWIR	PM	Combined
SPIN*	106.65	90.46	101.46	99.74
HMR	71.52	70.38	75.91	72.73
SPIN	66.27	67.00	70.32	67.82
HW-HuP	36.00	39.56	41.53	37.93

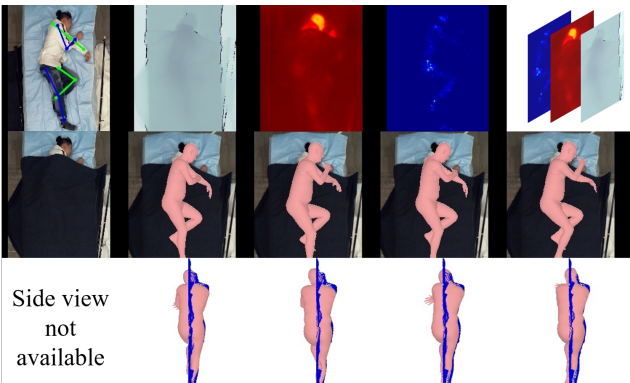


Fig. 5: Qualitative 3D human pose and shape estimation results of our HW-HuP model applied to an example image from SLP dataset with heavy occlusion (a thick blanket), under the respective input modalities of depth, long wavelength infrared (LWIR), pressure map (PM), and a combination of the three. First row shows the input modalities as well as a “Nocover” version of the RGB image as the reference. Second and third rows show the inference result of front view and side view, respectively.

lenging conditions, such as heavy occlusion and total darkness as previously considered in our work (Liu et al., 2023; Liu and Ostadabbas, 2019). In this study, we train HW-HuP on individual non-RGB modalities, by replacing the three RGB channels throughout the network with a single channel representing the new modality. The input modalities we

work with are long wavelength infrared (LWIR) data, pressure map (PM) data, and the depth data D itself. We also test the combined three-channel modality. Prediction performances under different cover conditions and modalities in Table 2 show that HW-HuP is still effective under these challenging conditions. As expected, performance is best without the cover, but still reasonable in the other settings. Since the depth is also used to determine the error, it is not surprising that the depth modality results are the strongest. A qualitative result example is shown in Fig. 5, and more comprehensive results are presented in the *Supplementary Materials*.

Table 3: Comparison of HW-HuP with the SOTA based on the mean per joint position error (MPJPE) metric after Procrustes analysis (PA) alignment with tested on Human3.6M dataset. HW-HuP performance is comparable to the SOTA with or without using ground truth 3D poses for training supervision. Approaches on the top part require no image with 3D ground truth, while approaches on the bottom part make use of 3D ground truth too. **Best PA MPJPE scores per data context in bold.**

Method	Uses Paired 3D	PA MPJPE
Lassner (Lassner et al., 2017)	No	93.9
Simplify (Bogo et al., 2016)	No	82.3
Pavlakos et al. (Pavlakos et al., 2018)	No	75.9
HMR (unpaired) (Kanazawa et al., 2018)	No	66.5
SPIN (unpaired) (Kolotouros et al., 2019a)	No	62.0
HW-HuP (ours)	No	50.4
NBF (Omran et al., 2018)	Yes	59.9
HMR (Kanazawa et al., 2018)	Yes	56.8
SPIN (Kolotouros et al., 2019a)	Yes	41.1
DSD (Sun et al., 2019b)	Yes	44.3
I2L (Moon and Lee, 2020)	Yes	41.1
Pose2Mesh (Choi et al., 2020)	Yes	46.3
Song et al. (Song et al., 2020) (w/2D kpts.)	Yes	56.4
VIBE (Kocabas et al., 2020) (temporal)	Yes	41.5

4.5 Large-Scale 3D Human Pose Benchmarks

To quantify HW-HuP performance in a setting with 3D ground truth data, we test it on Human3.6M combined with MPII 2D data (Andriluka et al., 2014) and compared its mean per joint position error (MPJPE) after Procrustes analysis (PA) alignment with reported results from SOTA approaches in Table 3. When images without 3D annotation is not available, HW-HuP performs noticeably better over the SOTA. In settings where 3D annotation is available, we note that HW-HuP nonetheless performs better than many SOTA models despite their use of the additional 3D data, and is not too far behind the top 3D enabled models, SPIN (Kolotouros et al., 2019a) and I2L (Moon and Lee, 2020), achieving only 50.4 mm error compared to their 41.1 mm. To be clear, by design, HW-HuP does not make use of the 3D annotations—the main purpose of this comparison is to quantify the bias of HW-HuP predictions when 3D pose data is not available.

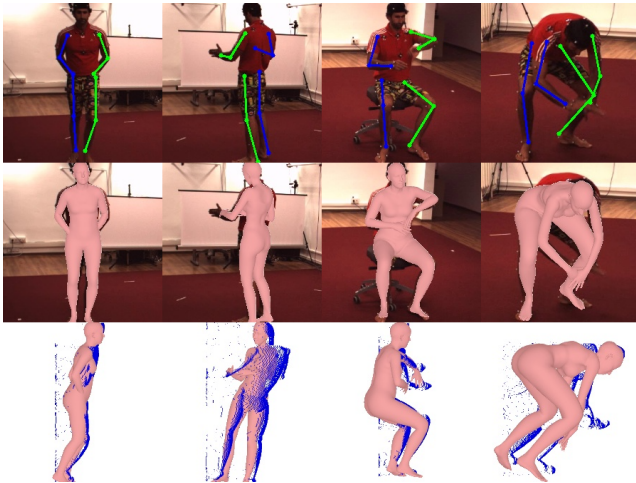


Fig. 6: Qualitative 3D human pose and shape estimation results of our HW-HuP applied to the Human3.6m validation dataset. The first row shows the input RGB images, the second and 3rd rows show HW-HuP pose predictions from the front and side view. Point clouds are rendered in blue dots for references. More visualization examples are displayed in the *Supplementary Materials*.

Table 4: Comparison of HW-HuP with the SOTA on the 3DPW dataset, based on the MPJPE metric. Note that HW-HuP does not use 3D ground truth training data, while the other models do. **Best PA MPJPE scores per data context in bold.**

Method	Uses 3D	MPJPE	PA-MPJPE
HMR (Kanazawa et al., 2018)	Yes	-	81.3
GraphCMR (Kolotouros et al., 2019b)	Yes	-	70.2
SPIN (Kolotouros et al., 2019a)	Yes	-	59.2
Pose2Mesh (Choi et al., 2020)	Yes	89.2	58.9
I2LMeshNet (Moon and Lee, 2020)	Yes	93.2	57.7
VIBE (Kocabas et al., 2020)	Yes	82.0	51.9
METRO (Lin et al., 2021a)	Yes	77.1	47.9
Mesh Graphormer (Lin et al., 2021b)	Yes	74.7	45.6
HW-HuP	No	-	66.1

Some HW-HuP pose predictions on Human3.6M are exhibited in Fig. 6. The predicted models have good 2D projected alignment on the RGB images, and also match ground truth point clouds quite closely, despite being produced without any ground truth 3D keypoint supervision.

We also test this model’s performance on the 3D human pose in the wild (3DPW) benchmark (von Marcard et al., 2018), which focuses on natural outdoor settings. The results in Table 4 show HW-HuP attaining comparable performance with SOTA approaches despite their full access to the 3D pose ground truth during training.

4.6 Infant 3D Pose Estimation

The analysis of infant motor activity plays a key role in the study of early childhood development (Prechtl, 1990; Hadders-Algra et al., 1997; Zwaigenbaum et al., 2013; Hesse

et al., 2018a), and accurate 3D infant pose estimation could enable automation of such analysis. We employ HW-HuP for this challenge, substituting the adult SMPL body model for the infant SMIL model (Hesse et al., 2018b), and testing the result on the MIMM and SyRIP datasets. Note that although statistical infant models are proposed in (Hesse et al., 2019, 2018b), they do not discuss how to estimate infant pose directly from a RGB image. Rather, they work with sequential RGBD input for both training and inference, and also require a specially configured physical setup to ensure that the infant point cloud can be easily segmented. By comparison, our training can take data from any RGBD setup in the wild, and we only require RGB images for subsequent inference. HW-HuP shows aligned depth error on MIMM is 42.0mm against the 58.14mm pretrained SPIN* and 46.2mm on fine tuned SPIN (Kolotouros et al., 2019a). Some qualitative results from both MIMM and SyRIP are shown in Fig. 7, demonstrating that HW-HuP is able to capture the infant 3D poses in clinical environments as well as in the wild.

5 Conclusion

We have introduced a transfer learning strategy for 3D human pose estimation in situations where neither ground truth 3D annotations nor learned priors are available. By selectively learning from source priors and easy-to-access observations in the target domain, our HW-HuP model yields robust 3D pose estimation performance even under challenging conditions. Since HW-HuP relies only on off-the-shelf depth cameras for training, it has the potential to solve a range of 3D human pose problems in real settings where MoCap training data is infeasible. Possible examples include patient monitoring in medical facilities, infant movement analysis in bassinets or cribs, pilot training observation in the cockpits, and driver behavior or gesture recognition inside of cars.

6 Acknowledgements

This material is based upon work supported by the National Science Foundation under Grant No. 1755695.

References

Andriluka M, Pishchulin L, Gehler P, Schiele B (2014) 2d human pose estimation: New benchmark and state of the art analysis. In: Proceedings of the IEEE Conference on computer Vision and Pattern Recognition, pp 3686–3693

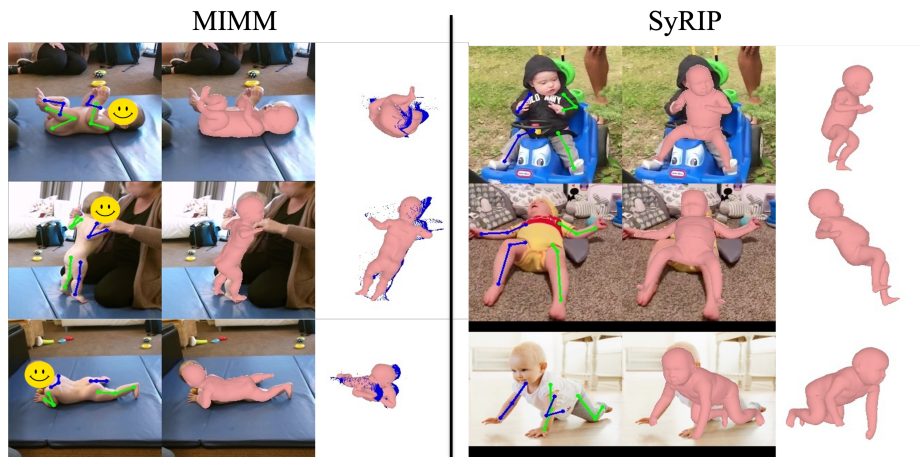


Fig. 7: Qualitative 3D human pose and shape estimation results of our HW-HuP model applied on the MIMM and SyRIP infant datasets. The first column shows the input RGB image. The second and third columns visualize the HW-HuP results of front and side views, respectively. Point clouds (blue dots) are aligned with side view model for MIMM result.

Bogo F, Black MJ, Loper M, Romero J (2015) Detailed full-body reconstructions of moving people from monocular rgb-d sequences. In: Proceedings of the IEEE international conference on computer vision, pp 2300–2308 [2](#)

Bogo F, Kanazawa A, Lassner C, Gehler P, Romero J, Black MJ (2016) Keep it smpl: Automatic estimation of 3d human pose and shape from a single image. In: European conference on computer vision, Springer, pp 561–578 [2](#), [3](#), [5](#), [7](#), [16](#)

Chen CH, Ramanan D (2017) 3d human pose estimation= 2d pose estimation+ matching. In: Proceedings of the IEEE Conference on Computer Vision and Pattern Recognition, pp 7035–7043 [2](#)

Cheng Y, Yang B, Wang B, Yan W, Tan RT (2019) Occlusion-aware networks for 3d human pose estimation in video. In: Proceedings of the IEEE/CVF International Conference on Computer Vision, pp 723–732 [16](#)

Cheng Y, Yang B, Wang B, Tan RT (2020) 3d human pose estimation using spatio-temporal networks with explicit occlusion training. In: Proceedings of the AAAI Conference on Artificial Intelligence, vol 34, pp 10631–10638 [16](#)

Choi H, Moon G, Lee KM (2020) Pose2mesh: Graph convolutional network for 3d human pose and mesh recovery from a 2d human pose. In: European Conference on Computer Vision, Springer, pp 769–787 [7](#), [8](#)

Clever HM, Erickson Z, Kapusta A, Turk G, Liu K, Kemp CC (2020) Bodies at rest: 3d human pose and shape estimation from a pressure image using synthetic data. In: Proceedings of the IEEE/CVF Conference on Computer Vision and Pattern Recognition, pp 6215–6224 [1](#), [5](#)

Dai W, Yang Q, Xue GR, Yu Y (2007) Boosting for transfer learning. In: Proceedings of the 24th international conference on Machine learning, ACM, pp 193–200 [1](#)

De Aguiar E, Theobalt C, Stoll C, Seidel HP (2007) Markerless deformable mesh tracking for human shape and motion capture. In: 2007 IEEE Conference on Computer Vision and Pattern Recognition, IEEE, pp 1–8 [2](#)

Fang HS, Xu Y, Wang W, Liu X, Zhu SC (2018) Learning pose grammar to encode human body configuration for 3d pose estimation. In: Thirty-Second AAAI Conference on Artificial Intelligence [16](#)

Geman S (1987) Statistical methods for tomographic image reconstruction. *Bull Int Stat Inst* 4:5–21 [5](#)

Gower JC (1975) Generalized procrustes analysis. *Psychometrika* 40(1):33–51 [16](#)

Hadders-Algra M, Van den Nieuwendijk AWK, Maitijn A, van Eykern LA (1997) Assessment of general movements: towards a better understanding of a sensitive method to evaluate brain function in young infants. *Developmental Medicine & Child Neurology* 39(2):88–98 [8](#)

Haque A, Peng B, Luo Z, Alahi A, Yeung S, Fei-Fei L (2016) Towards viewpoint invariant 3d human pose estimation. In: European Conference on Computer Vision, Springer, pp 160–177 [2](#)

Hassan M, Choutas V, Tzionas D, Black MJ (2019) Resolving 3d human pose ambiguities with 3d scene constraints. In: Proceedings of the IEEE/CVF International Conference on Computer Vision, pp 2282–2292 [2](#)

He K, Zhang X, Ren S, Sun J (2016) Deep residual learning for image recognition. In: Proceedings of the IEEE conference on computer vision and pattern recognition, pp 770–778 [13](#)

Helten T, Baak A, Bharaj G, Müller M, Seidel HP, Theobalt C (2013) Personalization and evaluation of a real-time depth-based full body tracker. In: 2013 International Conference on 3D Vision-3DV 2013, IEEE, pp 279–286 [2](#)

- Hesse N, Schröder AS, Müller-Felber W, Bodensteiner C, Arens M, Hofmann UG (2017) Body pose estimation in depth images for infant motion analysis. In: 2017 39th Annual International Conference of the IEEE Engineering in Medicine and Biology Society (EMBC), IEEE, pp 1909–1912 [1](#)
- Hesse N, Bodensteiner C, Arens M, Hofmann UG, Weinberger R, Sebastian Schroeder A (2018a) Computer vision for medical infant motion analysis: State of the art and rgb-d data set. In: Proceedings of the European Conference on Computer Vision (ECCV) Workshops, pp 0–8 [8](#)
- Hesse N, Pujades S, Romero J, Black MJ, Bodensteiner C, Arens M, Hofmann UG, Tacke U, Hadders-Algra M, Weinberger R, et al. (2018b) Learning an infant body model from rgb-d data for accurate full body motion analysis. In: International Conference on Medical Image Computing and Computer-Assisted Intervention, Springer, pp 792–800 [8](#)
- Hesse N, Pujades S, Black MJ, Arens M, Hofmann UG, Schroeder AS (2019) Learning and tracking the 3d body shape of freely moving infants from rgb-d sequences. *IEEE transactions on pattern analysis and machine intelligence* 42(10):2540–2551 [2](#), [8](#)
- Huang X, Rezaei B, Ostadabbas S (2019) AH-CoLT: an AI-Human Co-Labeling Toolbox to Augment Efficient Groundtruth Generation. In: IEEE 29th International Workshop on Machine Learning for Signal Processing (MLSP), pp 1–6 [2](#)
- Huang X, Fu N, Liu S, Ostadabbas S (2021) Invariant representation learning for infant pose estimation with small data. In: IEEE International Conference on Automatic Face and Gesture Recognition (FG), 2021 [5](#)
- Ionescu C, Papava D, Olaru V, Sminchisescu C (2013) Human3.6m: Large scale datasets and predictive methods for 3d human sensing in natural environments. *IEEE transactions on pattern analysis and machine intelligence* 36(7):1325–1339 [5](#), [13](#)
- Iskakov K, Burkov E, Lempitsky V, Malkov Y (2019) Learnable triangulation of human pose. In: Proceedings of the IEEE/CVF International Conference on Computer Vision, pp 7718–7727 [16](#)
- Kanazawa A, Black MJ, Jacobs DW, Malik J (2018) End-to-end recovery of human shape and pose. In: Proceedings of the IEEE Conference on Computer Vision and Pattern Recognition, pp 7122–7131 [5](#), [6](#), [7](#), [8](#), [15](#)
- Kato H, Ushiku Y, Harada T (2018) Neural 3d mesh renderer. In: The IEEE Conference on Computer Vision and Pattern Recognition (CVPR) [4](#), [5](#)
- Kingma DP, Ba J (2014) Adam: A method for stochastic optimization. *arXiv preprint arXiv:1412.6980* [5](#)
- Kocabas M, Athanasiou N, Black MJ (2020) Vibe: Video inference for human body pose and shape estimation. In: Proceedings of the IEEE/CVF Conference on Computer Vision and Pattern Recognition, pp 5253–5263 [7](#), [8](#)
- Kolotouros N, Pavlakos G, Black MJ, Daniilidis K (2019a) Learning to reconstruct 3d human pose and shape via model-fitting in the loop. In: Proceedings of the IEEE/CVF International Conference on Computer Vision, pp 2252–2261 [3](#), [5](#), [6](#), [7](#), [8](#), [15](#), [16](#)
- Kolotouros N, Pavlakos G, Daniilidis K (2019b) Convolutional mesh regression for single-image human shape reconstruction. In: Proceedings of the IEEE/CVF Conference on Computer Vision and Pattern Recognition, pp 4501–4510 [3](#), [8](#), [13](#)
- Lan Zz, Bao L, Yu SI, Liu W, Hauptmann AG (2012) Double fusion for multimedia event detection. In: International Conference on Multimedia Modeling, Springer, pp 173–185 [2](#)
- Lassner C, Romero J, Kiefel M, Bogo F, Black MJ, Gehler PV (2017) Unite the people: Closing the loop between 3d and 2d human representations. In: Proceedings of the IEEE conference on computer vision and pattern recognition, pp 6050–6059 [7](#)
- Li R, Cai C, Georgakis G, Karanam S, Chen T, Wu Z (2019) Towards robust rgb-d human mesh recovery. *arXiv preprint arXiv:1911.07383* [2](#)
- Lin K, Wang L, Liu Z (2021a) End-to-end human pose and mesh reconstruction with transformers. In: Proceedings of the IEEE/CVF Conference on Computer Vision and Pattern Recognition, pp 1954–1963 [8](#)
- Lin K, Wang L, Liu Z (2021b) Mesh graphormer. *arXiv preprint arXiv:2104.00272* [8](#)
- Lin TY, Maire M, Belongie S, Hays J, Perona P, Ramanan D, Dollár P, Zitnick CL (2014) Microsoft coco: Common objects in context. In: European conference on computer vision, Springer, pp 740–755 [13](#)
- Liu S, Ostadabbas S (2019) Seeing under the cover: A physics guided learning approach for in-bed pose estimation. In: International Conference on Medical Image Computing and Computer-Assisted Intervention, Springer, pp 236–245 [7](#)
- Liu S, Chen C, Kehtarnavaz N (2016) A computationally efficient denoising and hole-filling method for depth image enhancement. In: Real-time image and video processing 2016, International Society for Optics and Photonics, vol 9897, p 98970V [5](#)
- Liu S, Huang X, Fu N, Li C, Su Z, Ostadabbas S (2023) Simultaneously-collected multimodal lying pose dataset: Enabling in-bed human pose monitoring. *IEEE Transactions on Pattern Analysis and Machine Intelligence* 45(1):1106–1118, DOI 10.1109/TPAMI.2022.3155712 [1](#), [2](#), [5](#), [7](#), [13](#), [14](#)
- Loper M, Mahmood N, Romero J, Pons-Moll G, Black MJ (2015) Smpl: A skinned multi-person linear model. *ACM transactions on graphics (TOG)* 34(6):1–16 [3](#)

- von Marcard T, Henschel R, Black M, Rosenhahn B, Pons-Moll G (2018) Recovering accurate 3d human pose in the wild using imus and a moving camera. In: European Conference on Computer Vision (ECCV) 5, 8
- Martinez J, Hossain R, Romero J, Little JJ (2017) A simple yet effective baseline for 3d human pose estimation. In: Proceedings of the IEEE International Conference on Computer Vision, pp 2640–2649 16
- Mehta D, Rhodin H, Casas D, Fua P, Sotnychenko O, Xu W, Theobalt C (2017) Monocular 3d human pose estimation in the wild using improved cnn supervision. In: 2017 international conference on 3D vision (3DV), IEEE, pp 506–516 2
- Moon G, Lee KM (2020) I2l-meshnet: Image-to-lixel prediction network for accurate 3d human pose and mesh estimation from a single rgb image. In: Computer Vision—ECCV 2020: 16th European Conference, Glasgow, UK, August 23–28, 2020, Proceedings, Part VII 16, Springer, pp 752–768 7, 8
- Moon G, Chang JY, Lee KM (2019) Camera distance-aware top-down approach for 3d multi-person pose estimation from a single rgb image. In: Proceedings of the IEEE International Conference on Computer Vision, pp 10133–10142 16
- Nguyen CV, Izadi S, Lovell D (2012) Modeling kinect sensor noise for improved 3d reconstruction and tracking. In: 2012 second international conference on 3D imaging, modeling, processing, visualization & transmission, IEEE, pp 524–530 5
- Omran M, Lassner C, Pons-Moll G, Gehler P, Schiele B (2018) Neural body fitting: Unifying deep learning and model based human pose and shape estimation. In: 2018 international conference on 3D vision (3DV), IEEE, pp 484–494 7
- Park S, Hwang J, Kwak N (2016) 3d human pose estimation using convolutional neural networks with 2d pose information. In: European Conference on Computer Vision, Springer, pp 156–169 2
- Pavlakos G, Zhou X, Derpanis KG, Daniilidis K (2017) Coarse-to-fine volumetric prediction for single-image 3d human pose. In: Proceedings of the IEEE Conference on Computer Vision and Pattern Recognition, pp 7025–7034 2
- Pavlakos G, Zhu L, Zhou X, Daniilidis K (2018) Learning to estimate 3d human pose and shape from a single color image. In: Proceedings of the IEEE conference on computer vision and pattern recognition, pp 459–468 7
- Pavullo D, Feichtenhofer C, Grangier D, Auli M (2019) 3d human pose estimation in video with temporal convolutions and semi-supervised training. In: Proceedings of the IEEE/CVF Conference on Computer Vision and Pattern Recognition, pp 7753–7762 16
- Prechtl HF (1990) Qualitative changes of spontaneous movements in fetus and preterm infant are a marker of neurological dysfunction. *Early human development* 8
- Reddy ND, Guigues L, Pishchulin L, Eledath J, Narasimhan SG (2021) Tesseract: End-to-end learnable multi-person articulated 3d pose tracking. In: Proceedings of the IEEE/CVF Conference on Computer Vision and Pattern Recognition, pp 15190–15200 16
- Rhodin H, Salzmann M, Fua P (2018) Unsupervised geometry-aware representation for 3d human pose estimation. In: Proceedings of the European Conference on Computer Vision (ECCV), pp 750–767 2
- Rogez G, Weinzaepfel P, Schmid C (2017) Lcr-net: Localization-classification-regression for human pose. In: Proceedings of the IEEE Conference on Computer Vision and Pattern Recognition, pp 3433–3441 2
- Romera-Paredes B, Torr P (2015) An embarrassingly simple approach to zero-shot learning. In: International conference on machine learning, PMLR, pp 2152–2161 1
- Shotton J, Fitzgibbon A, Cook M, Sharp T, Finocchio M, Moore R, Kipman A, Blake A (2011) Real-time human pose recognition in parts from single depth images. In: CVPR 2011, Ieee, pp 1297–1304 2
- Song J, Chen X, Hilliges O (2020) Human body model fitting by learned gradient descent. In: European Conference on Computer Vision, Springer, pp 744–760 7
- Sun K, Xiao B, Liu D, Wang J (2019a) Deep high-resolution representation learning for human pose estimation. In: Conference on Computer Vision and Pattern Recognition (CVPR) 13
- Sun Y, Ye Y, Liu W, Gao W, Fu Y, Mei T (2019b) Human mesh recovery from monocular images via a skeleton-disentangled representation. In: Proceedings of the IEEE/CVF International Conference on Computer Vision, pp 5349–5358 7
- Tung HYF, Harley AW, Seto W, Fragkiadaki K (2017) Adversarial inverse graphics networks: Learning 2d-to-3d lifting and image-to-image translation from unpaired supervision. In: 2017 IEEE International Conference on Computer Vision (ICCV), IEEE, pp 4364–4372 2
- Xiao B, Wu H, Wei Y (2018) Simple baselines for human pose estimation and tracking. In: European Conference on Computer Vision (ECCV) 13
- Xiong F, Zhang B, Xiao Y, Cao Z, Yu T, Zhou JT, Yuan J (2019) A2j: Anchor-to-joint regression network for 3d articulated pose estimation from a single depth image. In: Proceedings of the IEEE/CVF International Conference on Computer Vision, pp 793–802 2
- Yang Y, Ramanan D (2013) Articulated human detection with flexible mixtures of parts. *IEEE Transactions on Pattern Analysis and Machine Intelligence* 35(12):2878–2890, DOI 10.1109/TPAMI.2012.261 14

- Ye M, Yang R (2014) Real-time simultaneous pose and shape estimation for articulated objects using a single depth camera. In: Proceedings of the IEEE Conference on Computer Vision and Pattern Recognition, pp 2345–2352 [2](#)
- Yu T, Guo K, Xu F, Dong Y, Su Z, Zhao J, Li J, Dai Q, Liu Y (2017) Bodyfusion: Real-time capture of human motion and surface geometry using a single depth camera. In: Proceedings of the IEEE International Conference on Computer Vision, pp 910–919 [2](#)
- Zhou X, Leonardos S, Hu X, Daniilidis K (2015) 3d shape estimation from 2d landmarks: A convex relaxation approach. In: proceedings of the IEEE conference on computer vision and pattern recognition, pp 4447–4455 [2](#)
- Zhou X, Zhu M, Leonardos S, Daniilidis K (2016) Sparse representation for 3d shape estimation: A convex relaxation approach. *IEEE transactions on pattern analysis and machine intelligence* 39(8):1648–1661 [16](#)
- Zhou X, Zhu M, Pavlakos G, Leonardos S, Derpanis KG, Daniilidis K (2018) Monocap: Monocular human motion capture using a cnn coupled with a geometric prior. *IEEE transactions on pattern analysis and machine intelligence* 41(4):901–914 [16](#)
- Zimmermann C, Welschehold T, Dornhege C, Burgard W, Brox T (2018) 3d human pose estimation in rgb-d images for robotic task learning. In: 2018 IEEE International Conference on Robotics and Automation (ICRA), IEEE, pp 1986–1992 [2](#)
- Zwaigenbaum L, Bryson S, Garon N (2013) Early identification of autism spectrum disorders. *Behavioural brain research* 251:133–146 [8](#)

A Supplementary Materials

Our source code is included as part of our supplementary submission. Furthermore, we discuss here: (1) a qualitative comparison between the HW-HuP and pre-trained SOTA 3D pose estimation models, (2) the design and evaluation of the VisNet for joint visibility estimation, (3) the results of projected 2D pose estimation on the SLP dataset, (4) concepts pertaining to selective pose prior transfer, (5) the error distribution of the depth-based 3D proxy, (6) a detailed comparison with the SOTA on Human3.6M dataset, and finally, (7) additional qualitative results.

A.1 Qualitative Performance of SOTA Pre-trained Model

Given that many SOTA models already show satisfactory performance on large-scale 3D pose benchmarks such as Human3.6M [Ionescu et al. \(2013\)](#) and 3DPW [Kolotouros et al. \(2019b\)](#), one might wonder whether the pretrained models are already sufficient for real life applications, even without domain-specific fine-tuning. We examined this question qualitatively for in-bed images from the SLP dataset, where poses appear simpler. An illustrative example of the pretrained model performance is given in Fig. S1. Contrast this with the better performance of the SOTA models after fine-tuning in Fig. 1—although even with fine-tuning, HW-HuP achieves superior results.

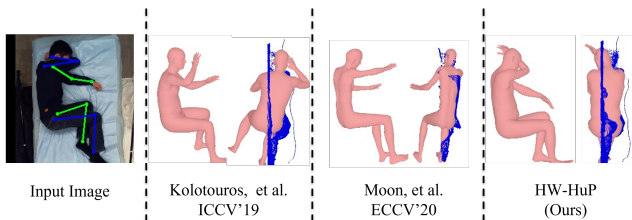


Fig. S1: Visual inspection of the accuracy of the 3D human pose and shape estimation pre-trained models compared to our heuristic weakly-supervised 3D human pose estimation model (HW-HuP), when applied on an in-bed pose image taken from the SLP dataset ([Liu et al., 2023](#)). Point clouds from depth are rendered in blue for reference. Compared to Fig. 1 in the main paper, the SOTA models here are not fine-tuned on SLP data.

A.2 VisNet for Joint Visibility Estimation

The main purpose of VisNet is to determine the visibility of joints in an image of a body. This issue has not featured extensively in existing pose estimation models since many such 3D models are trained on MoCap data, where visibility is not an issue, and otherwise pose estimation models are assumed to be capable of inferring the position of occluded

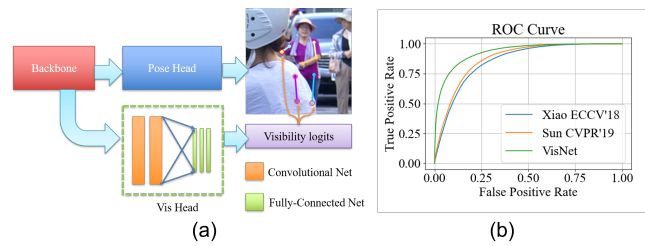


Fig. S2: (a) VisNet model diagram, and (b) visibility detection ROC performance on COCO validation dataset in, comparing VisNet visibility scores to confidence scores from ([Sun et al., 2019a](#); [Xiao et al., 2018](#)).

joints regardless. However, as discussed in Section 3, such occlusions can yield large biases in the depth-based proxy 3D joint coordinates used by HW-HuP to supervise its pose regression, precipitating the need for VisNet to filter out unreliable joints. In our design, the VisNet head is based on a ResNet [He et al. \(2016\)](#) backbone. It includes two convolution layers with 1×1 kernels and 256 and 32 channels respectively, followed by three fully connected layers with 256, 64, and 17 channels respectively. Each layer is followed by a batch normalization and a rectified linear unit (ReLU). To enhance its semantic understanding of the specific joint for visibility detection, we add the pose head [Xiao et al. \(2018\)](#) on top of the backbone for joint training. VisNet design is shown in Fig. S2(a). In our implementation, VisNet is trained with an Adam optimizer with learning rate of 0.001 with a total epoch of 80 trained on COCO dataset [Lin et al. \(2014\)](#), which contains visibility annotations.

As a simple baseline quantification of VisNet performance, we compare its predicted per joint visibility scores against the per joint prediction confidence scores obtained from two SOTA human pose estimation models [Xiao et al. \(2018\)](#); [Sun et al. \(2019a\)](#), with receiver operating characteristic curves shown in Fig. S2(b). With the area under the curve (AUC) of the ROC curve serving as our metric, VisNet scores 93.3%, higher than 85.6% from [Xiao et al. \(2018\)](#) and 87.5% from [Sun et al. \(2019a\)](#). Qualitative results of VisNet on COCO and Human3.6M [Ionescu et al. \(2013\)](#) are shown in Fig. S3. We observe that VisNet can more easily detect occlusions when the blocking and blocked objects have distinct appearances from each other. We also observe some common failures cases: (1) Visible joints can be wrongly classified as occluded when they are close to the boundary or to other objects, as with the image in Fig. S3 row 2, column 6. Presumably, sharp changes such as boundaries between objects or image boundaries are taken as clues of occlusion. (2) If the image only features partial views of the limbs, as in Fig. S3 row 1, column 6, the joints may be wrongly classified as occluded. (3) If one of the joints is occluded, the neighboring joints on the same limb are sometimes also deemed to be occluded, such as Fig. S3 (r2 c7).

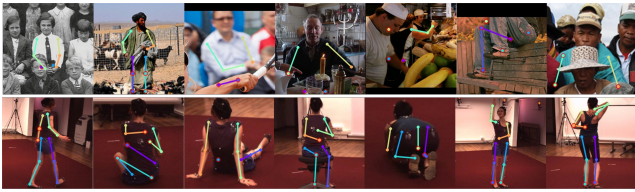


Fig. S3: Qualitative results of VisNet on COCO (first row) and Human3.6M (second row). Detected occlusions are annotated with red circle.

A.3 Projected 2D Pose Estimation Results on SLP

In Table 2 of the main paper, we demonstrated the superior performance of HW-HuP compared to SOTA on the SLP dataset by comparing their 3D pose predictions with the aligned depth error metric. Here, we offer another perspective on the same comparison, by projecting the 3D joint predictions of each model down to 2D and measuring the resulting percentage of correct keypoints (PCK) Yang and Ramanan (2013) relative to ground truth 2D annotations. Table S1 plots the results, with PCK correctness acceptance threshold of 20% of the body torso size (PCK@0.2). Since all models incorporate components of successful 2D pose estimators, the fine-tuned predictions are all quite strong. The results highlight the effectiveness of models using combined multimodal data under challenging conditions, which agrees with the results from Liu et al. (2023).

A.4 Comments on Selective Pose Prior Transfer

HW-HuP learning is guided by a source prior that fades as training on the target data progresses. Our ablation study shows the effectiveness of this feature when the SLP dataset is the target. One might wonder how such a mechanism can be effective—why not just learn directly from the target domain, which has a different pose distribution? In our experience, the source prior contribution mitigates the effect of *incompleteness* of the target domain due to limited observations and data. For example, the target domain might contain just enough information about major joint locations to regulate the placement of major body parts, but more subtle details such as axis rotations and the placement of small body parts are relatively unconstrained.

The visual examples in Fig. S1 show that models pre-trained on widely available human pose datasets tend to produce estimates of human poses that appear to be standing or squatting, even though the input images are of humans lying in bed. The main improvements from the HW-HuP estimate come from adjustment to major limbs, while rotation and placement of the head and hands are largely inherited from the source priors.

We can think of the source prior estimation and the true target pose as neighbours in the human pose manifold, with strong similarities in the small limbs. A pose guess from a source prior to regress to the target pose is always better than a guess from nowhere and we hope the evolution follows such a manifold. With a strong prior at beginning, the regressor F learns under the source prior guidance to learn the overall picture of full joint pose (rotation). As the source prior fades away, F will focus more on the observations from target domain to have its context-specific prior over the major joints yet keep the learned prior over the minor ones which is otherwise unconstrained under the target-only supervisions. In this way, the source pose prior is actually selectively transferred to the target regressor F .

Another benefit of the selective pose prior transfer, compared to transfer learning by continuing training of a pre-trained model, is that it is still helpful when the source and target domains use different input modalities, and so no pre-trained model in the target modality exists. Since the learned pose prior is modality independent, it can be used to guide learning even under a new modality.

A.5 Error Distribution from depth-based 3D proxy

Fig. S4 shows the error distributions resulting from using depth-based 3D proxy coordinates as estimates of the real proxy coordinates, in the training split of Human3.6M. We can see that biases tend to be larger at more distal joints, and smaller at proximal joints. This is in accordance to our assessment in the main text, that double- or multi-body occlusions are more likely at distal joints, leading to higher Type 2 errors.

A.6 Comprehensive Comparison with SOTA on Human3.6M

Table S2 is a more comprehensive version of Table 3, comparing HW-HuP with SOTA predictions on the Human3.6M.

A.7 More Qualitative Results

We exhibit further 3D prediction examples from the SLP dataset in Fig. S5 and from the Human3.6m dataset in Fig. S6. In Fig. S5, we include predicted results based on different input modalities (depth, LWIR, PM, or multi-modal) for subjects under different cover conditions (no cover, a thin layer sheet, or a thick blanket). Some failure cases are included such as in row 1, column 1, where LWIR fails, and also in row 3, column 1, where the left hand is not in a rest pose. For the visualization of Human3.6m frames in Fig. S6, we observe that although the performance of our HW-HuP model

Table S1: PCK@0.2 of HW-HuP and SOTA 3D joint predictions projected to 2D, compared to 2D ground truth, under “Nocover,” “Cover1,” “Cover2” and “All Covers” conditions and depth, LWIR, PM modalities in the SLP dataset.

Nocover					Cover1				
	Depth	LWIR	PM	Combined		Depth	LWIR	PM	Combined
SPIN* (Kolotouros et al., 2019a)	34.43	42.85	15.49	45.90	SPIN* (Kolotouros et al., 2019a)	19.63	17.21	15.82	24.58
HMR (Kanazawa et al., 2018)	96.51	95.57	90.59	95.46	HMR (Kanazawa et al., 2018)	90.76	91.93	90.71	94.14
SPIN (Kolotouros et al., 2019a)	96.23	95.57	90.56	95.45	SPIN (Kolotouros et al., 2019a)	90.37	92.21	90.51	94.17
HW-HuP	96.64	95.22	91.19	95.49	HW-HuP	91.70	91.90	91.20	94.21
Cover2					All Covers				
	Depth	LWIR	PM	Combined		Depth	LWIR	PM	Combined
SPIN* (Kolotouros et al., 2019a)	21.27	17.61	15.79	25.14	SPIN* (Kolotouros et al., 2019a)	25.11	25.89	15.70	31.87
HMR (Kanazawa et al., 2018)	91.17	91.53	90.80	93.38	HMR (Kanazawa et al., 2018)	92.81	93.01	90.70	94.33
SPIN (Kolotouros et al., 2019a)	90.83	91.94	90.34	93.33	SPIN (Kolotouros et al., 2019a)	92.48	93.24	90.47	94.32
HW-HuP	91.68	91.76	90.79	93.77	HW-HuP	93.34	92.96	91.06	94.49

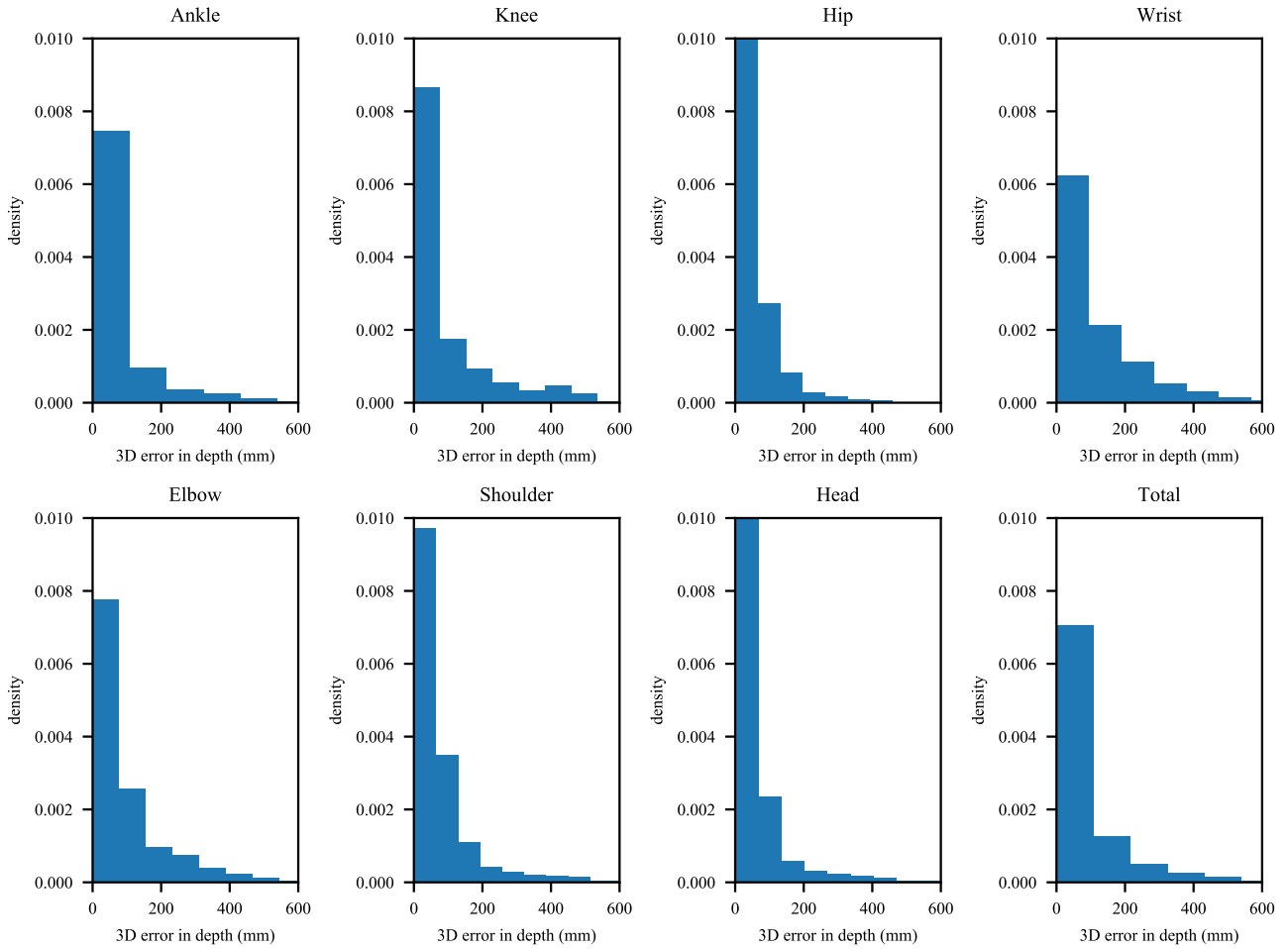


Fig. S4: Shift error distribution between depth-based 3D proxy and real proxy by joints of Human3.6M training split.

is comparable to the SOTA 3D pose estimation models, there are still some failure cases. For instance, the predicted upper limbs are more difficult to align to the point cloud than the lower limbs (e.g. as in the second pose of subject 9 and the fourth pose of subject 11).

Table S2: Comparison of HW-HuP with the SOTA based on the mean per joint position error (MPJPE) metric tested on Human3.6M dataset using Protocol#2, including some results with rigid Procrustes analysis (PA) alignment (Gower, 1975). HW-HuP performance is comparable to the SOTA despite not using ground truth 3D poses for training supervision. **Best MPJPE scores**, *best PA MPJPE scores*, and models (*) with further temporal constraints indicated.

Methods	Dir.	Dis.	Eat	Gre.	Phon.	Pose	Pur.	Sit	SitD.	Smo.	Phot.	Wait	Walk	WalkD.	WalkT.	Avg
Zhou et al. (Zhou et al., 2016)	99.7	95.8	87.9	116.8	108.3	107.3	93.5	95.3	109.1	137.5	106.0	102.2	106.5	110.4	115.2	106.7
SMPLify et al. (Bogo et al., 2016)	62.0	60.2	67.8	76.5	92.1	77.0	73.0	75.3	100.3	137.3	83.4	77.3	79.7	86.8	81.7	82.3
Zhou et al. (Zhou et al., 2018)	68.7	74.8	67.8	76.4	76.3	84.0	70.2	88.0	113.8	78.0	98.4	90.1	62.6	75.1	73.6	79.9
Martinez et al. (Martinez et al., 2017)	51.8	56.2	58.1	59.0	69.5	55.2	58.1	74.0	94.6	62.3	78.4	59.1	49.5	65.1	52.4	62.9
Sun et al. (Fang et al., 2018)	47.5	47.7	49.5	50.2	51.4	43.8	46.4	58.9	65.7	49.4	55.8	47.8	38.9	49.0	43.8	49.6
Moon et al. (Moon et al., 2019)	50.5	55.7	50.1	51.7	53.9	46.8	50.0	61.9	68.0	52.5	55.9	49.9	41.8	56.1	46.9	53.3
Iskakov et al. (monocular) (Iskakov et al., 2019)	41.9	49.2	46.9	47.6	50.7	57.9	41.2	50.9	57.3	74.9	48.6	44.3	41.3	52.8	42.7	49.9
Pavlo et al. * (Pavlo et al., 2019)	45.2	46.7	43.3	45.6	48.1	55.1	44.6	44.3	57.3	65.8	47.1	44.0	49.0	32.8	33.9	46.8
Cheng et al. * (Cheng et al., 2019)	38.3	41.3	46.1	40.1	41.6	51.9	41.8	40.9	51.5	58.4	42.2	44.6	41.7	33.7	30.1	42.9
Cheng et al. * (Cheng et al., 2020)	36.2	38.1	42.7	35.9	38.2	45.7	36.8	42.0	45.9	51.3	41.8	41.5	43.8	33.1	28.6	40.1
Reddy et al. * (Reddy et al., 2021)	38.4	46.2	44.3	43.2	44.8	48.3	52.9	36.7	45.3	54.5	63.4	44.4	41.9	46.2	39.9	44.6
SPIN et al. (Kolotouros et al., 2019a)	60.6	61.0	57.9	64.5	67.1	59.9	57.7	80.1	91.3	63.2	65.8	60.2	53.2	61.2	60.4	65.7
SPIN et al. PA	39.5	42.1	41.1	44.8	46.6	38.6	38.8	60.8	68.5	45.2	46.2	41.4	36.0	45.0	40.9	44.2
HW-HuP	95.0	103.9	99.8	101.0	106.3	94.2	110.1	121.4	140.1	103.3	112.8	99.5	92.8	107.2	101.9	104.1
HW-HuP PA	47.0	49.5	49.2	51.2	52.1	45.0	48.4	64.7	75.4	49.9	54.3	47.8	42.6	53.3	48.8	50.4

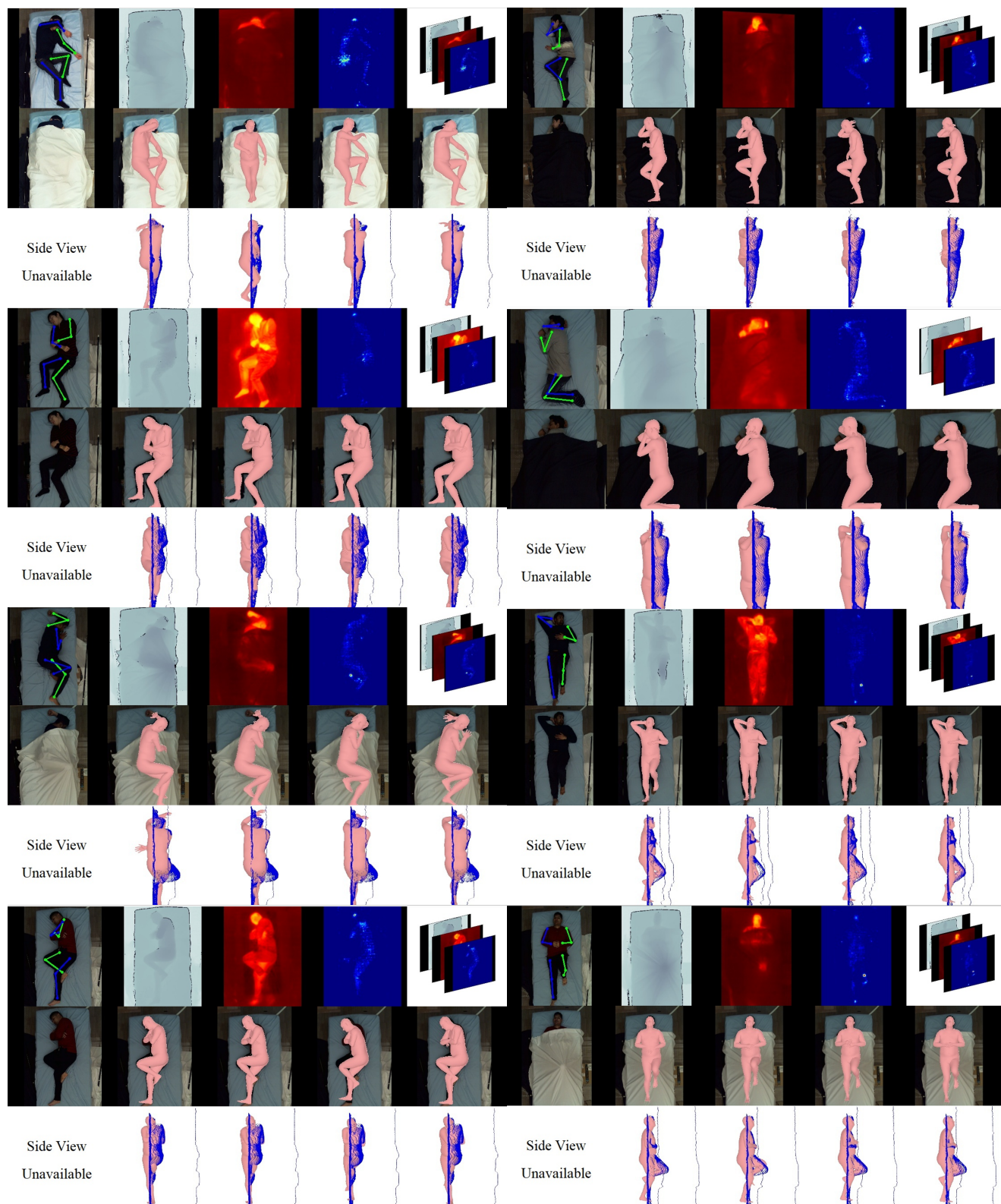


Fig. S5: Qualitative 3D human pose and shape estimation results of our HW-HuP applied to the SLP dataset, when input 2D images consist of the depth, LWIR, PM, modalities, or their combination, respectively. The row shows the input modalities as well as a “Nocover” version of the RGB image for reference. The second and third rows show the inference result of front view and side view, respectively.

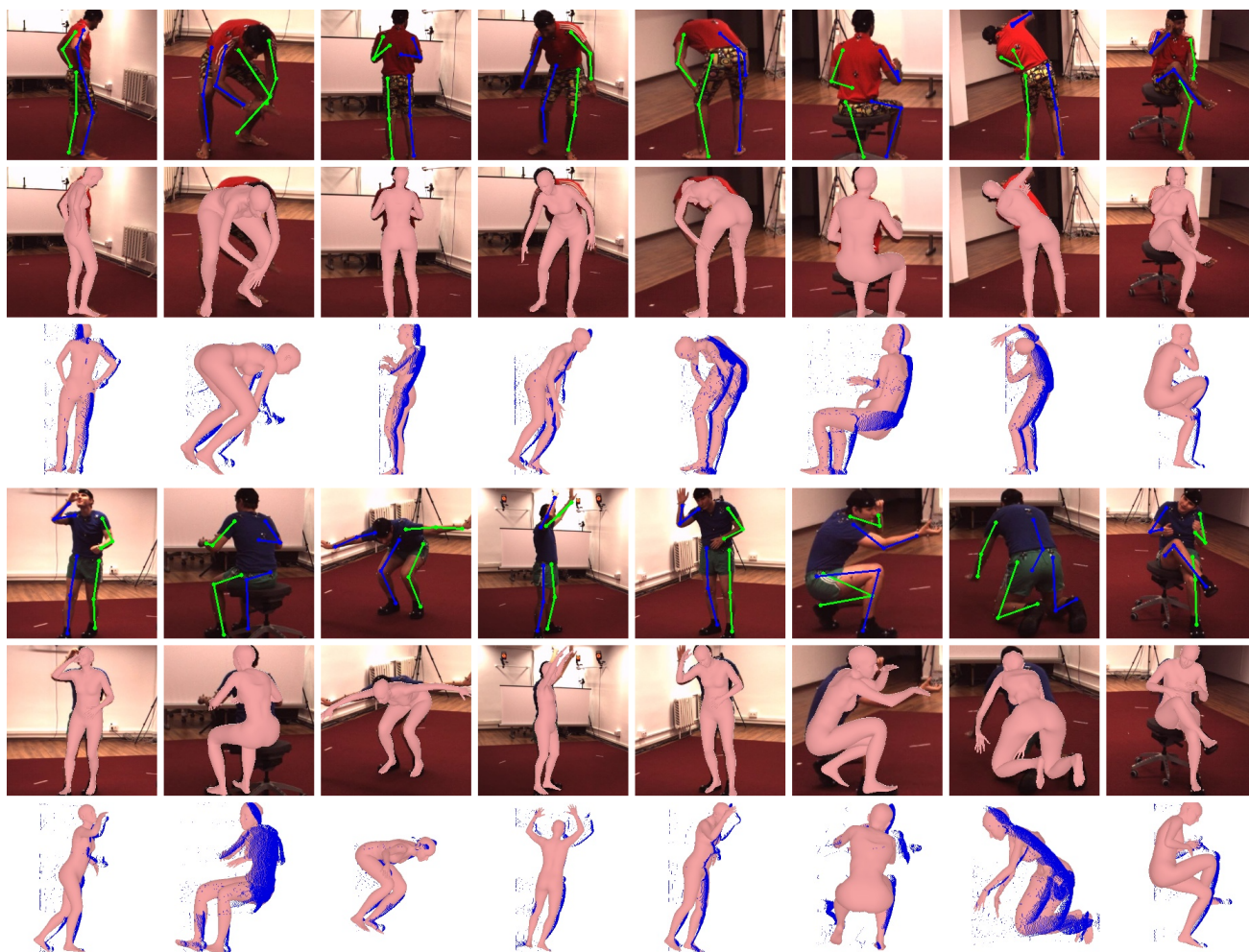


Fig. S6: More qualitative 3D human pose and shape estimation results of our HW-HuP applied to the Human3.6m validation dataset. The first three rows show the predictions of frames for subject 9, and the last three rows for subject 11.